A Protease-Responsive Polymer/Peptide Conjugate and Reversible Assembly of Silver Clusters for the Detection of *Porphyromonas gingivalis* Enzymatic Activity

Maurice Retout,
Department of Nano and Chemical Engineering, University of California, San Diego, La Jolla, California 92093, United States

Lubna Amer,
Materials Science and Engineering Program, University of California, San Diego, La Jolla, California 92093, United States

Wonjun Yim,
Materials Science and Engineering Program, University of California, San Diego, La Jolla, California 92093, United States

Matthew N. Creyer,
Department of Nano and Chemical Engineering, University of California, San Diego, La Jolla, California 92093, United States

Benjamin Lam,
Department of Nano and Chemical Engineering, University of California, San Diego, La Jolla, California 92093, United States

Diego F. Trujillo,
Skaggs School of Pharmacy and Pharmaceutical Sciences, University of California, San Diego, La Jolla, California 92093, United States

Jan Potempa,
Department of Microbiology, Faculty of Biochemistry, Biophysics and Biotechnology, Jagiellonian University, Krakow 30-387, Poland; Department of Oral Immunology and Infectious Diseases, School of Dentistry, University of Louisville, Louisville, Kentucky 40202, United States

Anthony J. O'Donoghue,
Skaggs School of Pharmacy and Pharmaceutical Sciences, University of California, San Diego, La Jolla, California 92093, United States

Casey Chen,
Herman Ostrow School of Dentistry, University of Southern California, Los Angeles, California 90089, United States

Corresponding Author Jesse V. Jokerst – Department of Nano and Chemical Engineering, University of California, San Diego, La Jolla, California 92093, United States; Materials Science and Engineering Program and Department of Radiology, University of California, San Diego, La Jolla, California 92093, United States; jjokerst@ucsd.edu.

Jesse V. Jokerst

Department of Nano and Chemical Engineering, University of California, San Diego, La Jolla, California 92093, United States; Materials Science and Engineering Program and Department of Radiology, University of California, San Diego, La Jolla, California 92093, United States

Abstract

We report the reversible aggregation of silver nanoparticle (AgNP) assemblies using the combination of a cationic arginine-based peptide and sulfur-capped polyethylene glycol (PEG). The formation and dissociation of the aggregates were studied by optical methods and electron microscopy. The dissociation of silver clusters depends on the peptide sequence and PEG size. A molecular weight of 1 kDa for PEG was optimal for the dissociation. The most important feature of this dissociation method is that it can operate in complex biofluids such as plasma, saliva, bile, urine, cell media, or even seawater without a significant decrease in performance. Moreover, the peptide–particle assemblies are highly stable and do not degrade (or express of loss of signal upon dissociation) when dried and resolubilized, frozen and thawed, or left in daylight for a month. Importantly, the dissociation capacity of PEG can be reduced via the conjugation of a peptide-cleavable substrate. The dissociation capacity is restored in the presence of an enzyme. Based on these findings, we designed a PEG-peptide hybrid molecule specific to the *Porphyromonas gingivalis* protease RgpB. Our motivation was that this bacterium is a key pathogen in periodontitis, and RgpB activity has been correlated with chronic diseases including Alzheimer's disease. The RgpB limit of detection was 100 pM RgpB *in vitro*. This system was used to measure RgpB in gingival crevicular fluid (GCF) samples with a detection rate of 40% with 0% false negatives versus PCR for *P. gingivalis* ($n = 37$). The combination of PEG-peptide and nanoparticles dissociation method allows the development of convenient protease sensing that can operate independently of the media composition.

Graphical Abstract
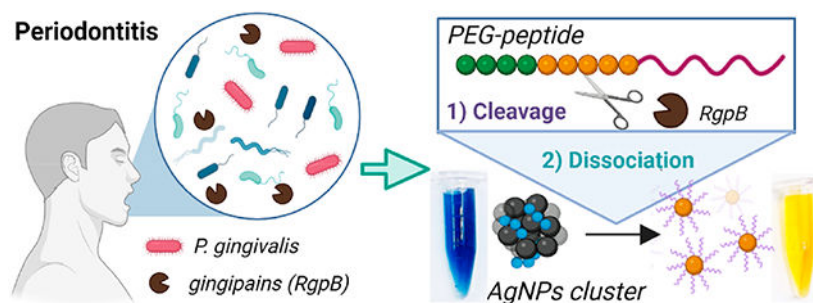
Keywords

silver nanoparticles; reversible assembly; protease sensing; PEG; peptides; P. gingivalis; periodontitis

INTRODUCTION

Periodontitis affects 46% of adults in the United States and costs billions of dollars in treatment annually.[1] Periodontitis causes irreversible destruction of tooth-supportive tissues and has been associated with rheumatoid arthritis and Alzheimer's disease.[2,3] Periodontitis is mainly caused by an imbalance in the oral microbiota and the resulting immune response.[4] Many of the periodontal pathogens are anaerobic, and among all, *Porphyromonas gingivalis* is the most studied because its presence has been correlated with disease progression with a prevalence of 78% in diseased subjects compared to 34% in healthy subjects.[5,6] *P. gingivalis* resides in the subgingival crevice, particularly in the gingival crevicular fluid (GCF), and due to its anaerobic metabolism, it secretes protease virulence factors (gingipains) that degrade extracellular proteins and modulate the host immune response.[7,8]

Gingipains are trypsin-like cysteine endopeptidases that can cleave peptides on the C-terminal of arginine.[9,10] They promote bacteria growth and lead to tissue destruction and chronic inflammation.[11] Gingipains represent more than 85% of the total proteolytic activity of *P. gingivalis*.[12] Thus, along with serving as a bacteria-presence signature, they are also relevant biomarkers of disease progression and development.[13] Gingipains are also associated with numerous systemic diseases such as cardiovascular,[14] arthritis,[15] diabetes,[16] and Alzheimer's disease (AD).[17]

However, there are almost no methods reported to monitor the activity of these proteases in patients. PCR is routine but difficult to do chairside.[18] Therefore, there is a clear need for point-of-care methods to detect and quantify the enzymatic activity of *P. gingivalis* that could, in turn, benefit both oral health and the treatment of systemic diseases related to periodontitis. Very few point-of-care methods have been reported that include plasmonic nanosensors[19] or fluorescence resonance energy transfer.[20]

Plasmonic nanostructures are a popular colorimetric reporter for the development of point-of-care *in vitro* diagnosis.[21,22] Their electronic properties generate a localized surface plasmon resonance (LSPR) band resulting in strong light absorption in the visible–infrared region.[23-25] Consequently, modulation of the LSPR band of plasmonic nanomaterials through variation of their shape, size, or dielectric environment can be exploited for biosensing.[26-29] One interesting strategy is the cross-linking of the nanoparticles in the presence of the analyte: Coupling of the individual LSPR bands lead to an unambiguous visual color change.[30-33] The aggregation of nanoparticles has been reported extensively,[34] but aggregation-based assays struggle to operate in complex environments such as biofluids.[29,35,36] They can aggregate nonspecifically due to charge screening or protein coronas.[37] The complex composition of the gingival crevicular fluid (GCF) (i.e., serum, leukocytes, structural cells, and oral bacteria) is thus a strong limitation to building traditional nanoparticle-based colorimetric sensors.

One approach to overcoming limitations in aggregation-based methods is to start with preassembled nanoparticles instead of a dispersed suspension. However, reversing the assembly of nanoparticles can be challenging due to the high attractive van der Waals forces that become incredibly high at small distances, maintaining the nanoparticles in

deep energetic minima.[38] However, we have recently shown that peptide-assembled gold nanoparticles (AuNPs) can be dissociated with a thiolated polyethylene glycol molecule (HS-PEG), thus generating a colorimetric signal indicative of the disassembly of the particles regardless of the matrix composition.[39]

Herein, we sought to extend this sensing mechanism to silver nanoparticles (AgNPs) because their extinction coefficient is 1 order of magnitude higher than that of AuNPs at equal size; thus, fewer AgNPs are needed to generate the same colorimetric signal which improves the sensitivity of the detection.[40,41] AgNPs are also much more sensitive to oxidation than AuNPs, making their handling more challenging because they dissolve and degrade more easily.[42-44] Although engineered surface modifications have been reported in the literature to protect the AgNPs,[40,45,46] they are still rarely used for *in vitro* diagnostics.

We thus envisioned that our reversible assembly strategy could be applied to AgNPs for the detection of *P. gingivalis* in GCF as it combines (i) the generation of a matrix-insensitive colorimetric signal with (ii) the peptide/HS-PEGs coating of AgNPs. We first characterized the reversible assembly of AgNPs with a cationic tripeptide, and we then designed a PEG-peptide probe responsive to gingipains that we used for the detection of clinical GCF samples.

RESULTS AND DISCUSSION

Characterization of the Reversible Assembly

We used citrate-capped AgNPs (AgNPs-citrate) and an RRK tripeptide (Arg-Arg-Lys) to form dense and compact yet reversible aggregates. We hypothesized that RRK and the citrate interact via electrostatic interactions and form a protective network surrounding the particles that prevent them from transitioning into a permanent aggregated state.[39] The assembly can thus be dissociated by using a stabilizing ligand with high affinity for the silver surface (i.e., a thiolated PEG methoxy, 1 kDa, HS-PEG-OMe (1 kDa)) (Figure 1A). Figure 1B shows the 3D structure of cationic tripeptide RRK.

A major advantage of assembling and disassembling plasmonic nanostructures is the ability to easily modulate the interaction between the individual LSPR bands. Figure 1C shows that the LSPR band of AgNPs deformed proportionally to the concentration of RRK with the appearance of a new peak at 620 nm and a decrease in the absorbance at 400 nm. Interestingly, the addition of HS-PEG-OMe (1 kDa) reversed the LSPR band deformation. Based on the LSPR band deformation, we defined the dissociation capacity as the ratio of the absorbance at 400 nm over that at 620 nm ($A_{.400nm}/A_{.620nm}$). Figure 1D and Figure 1E show that 10 μM RRK was sufficient to induce the maximal assembly of AgNPs and that similarly, approximately 10 μM HS-PEG-OMe (1 kDa) induced the complete dissociation.

The concentration of peptide needed to induce the particle assembly was directly influenced by the peptide sequence. Initial attempts to induce aggregation with a single arginine (R) proved ineffective (Figure 1). This observation agrees well with previous studies showing that multiple positively charged amino acids are necessary for particle aggregation.[35,47] Conversely, peptides containing two or three repetitions of RRK ((RRK)$_2$ and (RRK)$_3$)

required lower concentrations (<1 μM) to reach the same level of aggregation as RRK (Figure 1F). However, (RRK)$_2$ and (RRK)$_3$-induced assembly of AgNPs proved more challenging to dissociate; a higher concentration of HS-PEG-OMe (1 kDa) was needed (almost 1 order of magnitude higher for (RRK)$_3$ compared to RKK), and the dissociation efficiency was lower than for RRK (Figure 1G). This can be explained by the higher affinity of (RRK)$_2$ and (RRK)$_3$ for the citrate layer compared to RRK. Indeed, the reversible assembly works only if the citrate/peptide layer can be removed from the surface by the stabilizing ligand.[39]

Figure 1H shows the FTIR spectra of AgNPs-RRK and AgNPs-S-PEG-OMe (1 kDa). After dissociation, the absorbance at 1650 cm^{-1}, corresponding to a mixture of carboxyl and amide band signals, disappeared, while a new peak at 1100 cm^{-1} emerged due to C–O–C stretching of the PEG chain. This shows that the citrate/RRK layer was removed as the HS-PEG-OMe (1 kDa) grafted onto the surface, thus leading to dissociation. The addition of cationic peptides to AgNPs-citrate did not dissolve the particles or induce release of silver ions (Figure S1).

The reversible assembly of AgNPs was next characterized by multispectral advanced nanoparticles tracking analysis (MANTA)[48] and transmission electronic microscopy (TEM). The size of the AgNPs-RRK aggregates was approximately 170 nm, but this size decreased following HS-PEG-OMe (1 kDa) addition until it plateaued around 50 nm (Figure 1I). The initial size of the AgNPs-citrate was 40 nm, and the 50 nm size for AgNPs-S-PEG-OMe (1 kDa) agrees well with the presence of a PEG layer on the NP surface.[32] TEM analysis showed bulky and dense aggregates after the addition of RRK to AgNPs-citrate (Figure 1J). Interestingly, the addition of HS-PEG-OMe (1 kDa) led to the dissociation of the bulky aggregates into smaller ones until the concentration of HS-PEG-OMe (1 kDa) was sufficient to have only monodispersed particles (Figure 1J). See Supporting Information for TEM images at various magnifications (Figure S2).

The generation of the colorimetric signal associated with the NPs dissociation was then compared to AuNPs and evaluated in complex matrices. The strong deformation of the LSPR band of AgNPs during the dissociation (220 nm of blue shift) induced a change of color of the suspension from bright blue to yellow (Figure 2A). Alternatively, AuNPs provided a blue shift of only 130 nm (bright blue to red; Figure 2B). This larger shift in the maximum absorption caused a greater ratio of the absorbances for silver than gold (30 vs 10). This wider dynamic range is important because it implies a better sensitivity (Figure 2C). However, the kinetics of the dissociation were slower for AgNPs than AuNPs at an equal optical density (Figure 2D). For AgNPs the signal increased for 120 min, while for AuNPs, it stabilized after 15 min. This difference can be explained by the number of AgNPs that is 10 times lower than the one of AuNPs at the same optical density of 1. For convenience, we used 30 min as a standard measuring time for the remainder of this study. See Figure S3 for the dissociation kinetics at various concentrations.

The HS-PEG-induced dissociation of NP assembly could operate independently of the composition of the matrix. AgNPs-RRK assemblies were suspended in various media such as EBC, saliva, plasma, urine, cell medium (DMEM), bile, and even seawater. For each of

the samples, the media composition was 95% except for bile, which was limited to 20% due to its strong light absorption around 400 nm. For all the media, the addition of 20 μM HS-PEG-OMe (1 kDa) led to the dissociation of the particles characterized by a strong increase of their absorbance at 400 nm (Figure 2E). As a result, the suspensions turned bright yellow. An obvious color change was observed even in the case of light absorbing media such as plasma, urine, and bile (Figure 2F). The dissociation in complex biofluids did not require a higher concentration of HS-PEG-OMe (1 kDa) than in water; approximately 10 μM was sufficient to reach the dissociation plateau (Figure S4).

After the demonstration of the use of AgNPs-RRK in complex matrices, the stability and robustness of AgNPs-RRK assemblies were evaluated. Due to the protective layer formed by the citrate and RRK, it was possible to dry the particles on a solid surface and later solubilize and dissociate them after adding water with HS-PEG-OMe (1 kDa) (Figure 2G). This is particularly interesting in colorimetric sensing because it provides a great contrast between dried aggregates (clear) and dissociated suspensions (yellow). Similarly, the AgNPs-RRK could be either frozen and thawed or left on the bench in daylight for over a month without showing any loss of particles or dissociation capacity (Figure 2H). These findings illustrate the powerful storage potential of peptide-based AgNPs assemblies.

Effect of the PEG Structure on the Dissociation

The effect of the PEG structure on the dissociation of the assemblies was studied next: PEGs-OMe carrying anchoring groups other than thiol were tested: hydroxy (OH-PEG-OMe), alkyne (Alkyne-PEG-OMe), amine (NH_2-PEG-OMe), azide (N_3-PEG-OMe), and lipoic acid (LA-PEG-OMe) (Figures 3A and S6). For each, a molecular weight (mol wt) of 1 kDa was used. Unsurprisingly, OH-PEG-OMe could not dissociate the assemblies because the molecules do not have a functional group capable of binding to the surface of the NPs, i.e., no sulfur. Thus, there was no dissociation with alkyne-PEG-OMe, NH_2-PEG-OMe, and N_3-PEG-OMe. This was surprising because these groups can usually graft onto noble metal nanoparticles like gold nanoparticles. This finding indicates that only the thiol group can dissociate the silver cluster probably because the strength of the Ag—S bond is much higher than that of the other groups. Similarly, LA-PEG-OMe could not dissociate the assemblies, despite it having two sulfur atoms. Indeed, the two sulfur atoms are oxidized via a disulfide bond and cannot graft onto the silver surface. However, after reduction by (tris(2-carboxyethyl)phosphine (TCEP) and breaking of the disulfide bond into two thiol groups, LA-PEG-OMe does dissociate the assemblies dissociation. A lower concentration was required compared to single-thiol containing PEGs (i.e., HS-PEG-OMe) (Figure S6). This finding underscores the importance of thiol groups for assembly dissociation.

The second structural parameter that we studied was the size of the HS-PEGs. Here, MANTA, UV–vis spectroscopy, and TEM were used to monitor the dissociation as a function of the PEG size. HS-PEG-OMe with molecular weight varying from 20 kDa to 0.2 kDa was investigated. MANTA showed that the dissociation was directly related to the mol wt of HS-PEG-OMe: Low or very high mol wt (0.2 kDa and >5 kDa) could barely dissociate the aggregate (Figure 3B). UV–vis spectroscopy confirmed that there was a sweet spot for the dissociation at approximately 1 kDa with mol wt above 5 kDa and below 0.5

kDa having a low dissociation capacity (Figure 3C). This can be explained by the inability of large HS-PEG-OMe to penetrate the aggregates and thus stabilize individual particles. On the other hand, small HS-PEG-OMe can penetrate the assemblies but are too short to confer a good colloidal stability to the nanoparticles. See Figure S7 for titration curves with HS-PEG-OMe of various sizes.

TEM showed that the particles remained aggregated in the presence of HS-PEG-OMe with a mol wt of >5 kDa (Figures 3 D, S2, S8, and S9). The number of aggregates decreased as the size of the HS-PEG-OMe decreased; only individual particles could be observed for mol wt = 1 kDa. For lower mol wt (0.5 and 0.2 kDa), the number of aggregates started to increase again. HS-PEG-OMe (0.2 kDa) could dissociate the aggregate initially, but the particles recollapsed shortly thereafter, leading to dense aggregates. This is due to the inability of 0.2 kDa to sufficiently stabilize the particles.

The properties of the HS-PEGs can influence the dissociation of the AgNPs aggregates, and we envisioned that the conjugation of a peptide to HS-PEG could modulate its dissociation capacity. Importantly, if the peptide is a protease-cleavable substrate, then it would be possible to build a protease-responsive PEG-peptide conjugate where the dissociation capacity can only be restored by enzyme activity (Figure 4A).

Peptides containing the motif $(xxK)_n$ were synthesized, where x was either an alanine, an aspartic acid, or an arginine residue; n represents one, two, or three repetitive units (Figure 4B). See Table S1 for a summary of the peptide sequences and Figures S10 and S11 for corresponding chromatograms and ESI-MS spectra. All these peptides were conjugated to a HS-PEG carrying a carboxyl group (HS-PEG-COOH) with an average mol wt of 790 Da in order to elucidate the minimal size and/or mass required to prevent the dissociation. The conjugation was performed using an EDC/NHS cross-linking reaction between the carboxyl group of the HS-PEG-COOH and the lysine contained in the peptide sequences. MALDI-TOF was used to confirm the conjugation (Figure S13). All the HS-PEG-peptides were then titrated to the AgNPs-RRK clusters, and the dissociation ($A_{.400nm}/A_{.620nm}$) was evaluated.

An interesting correlation between the product mass × charge of the peptide and the dissociation capacity of the resulting HS-PEG-peptide (50 μM) was observed. Positively charged peptides instantly returned a strong decrease of the dissociation capacity of the PEG proportional to the mass × charge product (Figures 4C and S14). From a product of +4500, the dissociation capacity of the HS-PEG was completely turned off. Positively charged residues likely interact with PEG chains that contain numerous oxygen atoms and thus numerous electron lone pairs. This charge effect then combines with the size effects previously described to completely halt the potential for dissociation. For the negatively charged peptides, only the size effect was observed, and from a mass × product of −4500 the dissociation capacity was only decreased by 33%.

To our delight, the dissociation capacity of HS-PEG-(RRK)$_2$ and HS-PEG-(RRK)$_3$ could be turned on by trypsin digestion (Figures 4D and S15). Trypsin is an efficient enzyme that cleaves on the C-terminal side of arginine residues.[49] The cleavage induced the release

of the positively charged peptide from the HS-PEG, and thus its capacity to dissociate the aggregates was restored. Figure 4E,F shows TEM images of AgNPs-RRK mixed with either HS-PEG-(RRK)$_2$ or HS-PEG-(RRK)$_2$ digested with trypsin. The latter dissociated the assemblies, leading to a bright yellow color (Figure 4G).

Design of a PEG-Peptide Specific to Gingipains

We next developed a PEG-peptide responsive to gingipain (RgpB). We first incubated RgpB with an equimolar mixture of 228 highly diversified synthetic peptides that are each 14 amino acids in length. Cleavage at any one of the 2964 peptide bonds within this library can be detected and quantified by liquid chromatography–tandem mass spectrometry. This approach, termed multiplex substate profiling by mass spectrometry, has been used to generate substrate specificity profiles for more than 80 different proteases.[50] RgpB cleaved 83 out of 2964 peptide bonds after 10 min incubation with the peptide library. We analyzed the sequence of the amino acids surrounding the cleavage site and found that RgpB had a strong preference for cleaving between R and G with the sequence FLVRG (Supporting Information, section 2.4). We subsequently synthesized a PEG-peptide containing this RgpB cleavable sequence (Figure 5A). Peptide L1 (RRRGGFLVRGK) (Figure S16) was conjugated to a HS-PEG-COOH (790 Da) via the EDC/NHS cross-linking reaction. L1 had a mass of approximately 1300 Da and a charge of +4, and the product mass × charge was thus +5200. The lysine at the C-terminal was used for the conjugation, and the RgpB cleavable sequence (FLVR*G) was flanked with a glycine pair to enhance flexibility via spacing followed by three arginines to increase the overall positive charge and thus reach a mass × charge product of over 5000. HS-PEG-L1 was thus expected to be incapable of dissociating the AgNPs-RRK assembly due to the high mass × charge product of L1 conjugated to the HS-PEG. However, the cleavage by the enzyme removes almost all the peptide fragment.

First, MALDI-TOF mass spectrometry was used to confirm the conjugation: There was a clear defined peak at around 2100 Da (Figure 5B). More importantly, after 3 h of incubation with 200 nM recombinant RgpB, the signal from HS-PEG-L1 could not be observed anymore, and two new peaks emerged: one at 1157 Da and one at 964 Da that corresponded to peptide fragments RRRGGFLVR and GK-PEG-SH, respectively. This, in turn, confirmed that HS-PEG-L1 can be cleaved by RgpB. Indeed, HS-PEG-L1 was tested with the nanoparticles, and (as expected) no dissociation of either AgNPs-RRK or AuNPs-RRK assemblies was observed in the absence of cleavage even at concentrations of 100 μM due to its high mass × charge number (Figure 5C).

However, HS-PEG-L1 which was previously cleaved by RgpB (200 nM) could dissociate the assemblies from a minimum concentration of 10 μM, which is in good agreement with the required HS-PEG concentration determined previously. TEM confirmed that AgNPs-RRK mixed with the intact HS-PEG-L1 remained aggregated, while when mixed with the cleaved HS-PEG-L1, the particles dissociated (Figure 5D,E).

The limit of detection (LOD) of RgpB was then determined by incubating various concentrations with a constant concentration of HS-PEG-L1 (500 μM) for 2 h. Then, the resulting solution was added to the NPs-RRK assemblies for colorimetric analysis. A

LOD of approximately 100 pM was determined for AgNPs versus 100 nM for AuNPs (Figure 5F). These data highlight the superior sensitivity of silver nanoparticles versus gold nanoparticles in such systems due to their higher extinction coefficient and wider dynamic range. Incorporating AgNPs instead of AuNPs in sensing devices represents thus an advantage in terms of sensitivity and also costs less because nearly 10-fold fewer particles are needed to produce the same optical intensity. These advantages may have value for clinical applications.

Control experiments were conducted to demonstrate the specificity of the PEG-peptide probe for RgpbB (Figure 5G and Table 1). A peptide (**L2**) with missing arginines at the cleavage site (RRRGGFLVA**A**GK) was first synthesized and conjugated to HS-PEG-COOH. The resulting HS-PEG-L2 was incapable of dissociating the AgNPs-RRK assemblies after incubation with RgpB due to the absence of cleavage. The cleavage site is limited to the arginine in FLVRGK, and there is no nonspecific cleavage after the first three arginine residues. Increasing the number of arginine residues at the N-terminal extremity of the peptide (**L3**, RRRRRRGGFLVRGK) decreased the dissociation restoration after incubation with RgpB. This could be due to an excess of positive charge that hindered the dissociation or a lower cleavage efficiency from RgpB due to a change in the structure of the peptides. Indeed, **L1** initially has a β sheet secondary structure, while **L3** has an α helix structure (see Figure S17 for 3D structures of the peptides). Additional controls included RgpB (200 nM) inactivated by heating (70 °C for 1 h) and RgpB (200 nM) preincubated with leupeptin inhibitor (200 nM, 1 h).[51] No dissociation signal was generated in either case, thus confirming that the cleavage of the peptide is the trigger for dissociation.

Next, we investigated the ability of our platform to detect RgpB (200 nM) in complex media: human exhaled breath condensate (EBC), saliva, plasma, urine, and bile or cell media (DMEM), and even seawater. A strong colorimetric signal change associated with dissociation of the assemblies was obtained for every media excepted urine (Figure 5H; Figure S18).

Finally, HS-PEG-L1 and AgNPs-RRK assemblies were used for the detection of RgpB directly in bacteria cultures. *P. gingivalis* was grown on a blood agar plate, and colonies were transferred to broth and expanded to a concentration of 10^6 cells/mL. Then HS-PEG-L1 was incubated at 37 °C directly in the bacteria solution, and 3 h later, the AgNPs-RRK assemblies were added (Figure 5I). The color of the solution quickly turned bright yellow as the particles dissociated due to the cleavage by RgpB produced by *P. gingivalis* (Figure 5J). Control microorganisms were used to confirm the specificity of our method: the bacterium *F. nucleatum* and the fungus *C. albicans*. These microorganisms are good controls because they are also commonly identified in the gingival sulcus but do not express gingipains. Similar to *P. gingivalis*, both *F. nucleatum* and *C. albicans* were grown on a plate, transferred to broth, and expanded to reach a concentration of 10^6 cells/mL. The media used for *P. gingivalis/F. nucleatum* and *C. albicans* were different (details can be found in the Supporting Information section 2.12). As expected, no dissociation signal was obtained for either *F. nucleatum*, *C. albicans*, or their respective media because no RgpB was expressed. These findings confirm that this method can operate in very complex environments and there is high specificity of our HS-PEG-peptide probe toward RgpB.

Finally, the dissociation of AgNPs-RRK assemblies and HS-PEG-L1 were applied to the sensing of clinical GCF samples collected from 37 tooth sites in a set of 17 subjects, comprising both healthy patients and individuals with symptoms of periodontal disease (stage III periodontitis) sampled at a dental clinic. Figure 6A illustrates the GCF of diseased patients that contain *P. gingivalis* and gingipains. Samples were collected with a curet and stored in Tris buffer and glycerol (5%). Here, 5 μL of each clinical sample was mixed with 5 μL of HS-PEG-L1 (1 mM) and incubated for 3 h before the mixture was added to 100 μL of AgNPs-RRK assemblies, and the colorimetric signal was recorded. Each sample was assayed simultaneously with both qPCR and our system. Of these, 75% contained *P. gingivalis* (18/24) via qPCR and were thus considered positive (Figure 6B). The gingipain activity via our dissociation method was correlated with the qPCR results, despite a lower sensitivity: Seven samples were detected over the 18 positives corresponding to a 40% detection rate (Figure 6C). There were no negative samples coming from either the healthy (0/13) or diseased (0/6) patients corresponding to a 0% false positive rate (Figure 6D). qPCR is not a direct measurement of gingipain activity, and it reflects only the amount of total bacterial cells including live, live but senile, and dead cells. Only metabolically active cells (live) express gingipains.

Overall, the gingipain activity was much higher for GCF from patients with periodontitis of stage III compared to healthy patients, which confirms our method as promising for the development of point-of-care bacterial enzyme sensing (Figure 6E).

CONCLUSION

Herein we report the dissociation of RRK-induced AgNPs assemblies using HS-PEGs stabilizing ligands. After systematic characterization of the system, we found no degradation of the particles during the assembly. The particles could be dissociated as a function of the HS-PEG size. Moreover, the conjugation of a peptide possessing sufficient size and positive charges to the HS-PEGs resulted in the dissociation capacity being turned off. Importantly, the dissociation capacity could be restored by the removal of the peptide moieties from the HS-PEG after an enzymatic cleavage. We thus extended this concept for the detection of *P. gingivalis* enzymatic activity. A PEG-peptide probe specific to *P. gingivalis* enzymes (gingipains, RgpB) was designed and applied for the detection of recombinant RgpB. A limit of detection of 100 pM was obtained with AgNPs which was >100 times more sensitive than similar gold nanoparticle systems. Finally, our detection platform was applied to the sensing of clinical GCF samples. A detection of 40% of the positive diagnosed samples was obtained associated with a 0% false positive rate. The combination of PEG-peptide and AgNPs dissociation is thus promising for the development of matrix-insensitive colorimetric sensing of proteases. We imagine that this colorimetric gingipain assay may have value in chairside analysis of periodontal health on a tooth-by-tooth basis to quickly identify the extent of *P. gingivalis* involvement. Furthermore, the changes in optical absorbance could be used to produce photoacoustic signal to map and measure gingipains in the periodontal pocket or even in the brain for studies of Alzheimer's etiology.[3,20] Intraoral imaging would use customized and miniaturized equipment under development in our laboratory.[52] Importantly, this sensing strategy can be extended to

any other enzyme after identification of the proper peptide substrate with conjugation to HS-PEGs.

EXPERIMENTAL SECTION

Reversible Assembly of AgNPs

100 μL of 20 nm AgNPs-citrate (OD = 2, 0.4 nM) was mixed with 20 μM RRK in aqueous solution. Immediately, the color of the suspension turned from bright yellow to orange and then red. After 20 min, the color was bright blue, and the particles were assembled and ready for dissociation. To do so, 20 μM HS-PEG-OMe was added to the AgNPs-RRK. Rapidly, the color of the suspension turned from bright blue to purple and then red. After 30 min, the reaction was completed, and the color of the suspension returned to bright yellow.

Peptide Synthesis

Peptides were synthesized using an automated Eclipse peptide synthesizer (AAPPTec, Louisville, KY) through standard solid phase Fmoc synthesis on Rink-amide resin. Peptides were lyophilized in a FreeZone Plus 2.5 freeze-dry system (Labconco Corp., Kansas, MO) and purified with a Shimadzu LC-40 HPLC system equipped with a LC-40D solvent delivery module, photodiode array detector SPD-M40, and degassing unit DGU-403. Fractions containing the pure peptide, as confirmed by electrospray ionization mass spectrometry (ESI-MS, positive ion mode), were lyophilized and aliquoted. The RgpB specific peptide substrates were determined using a multiplex substrate profiling by a mass spectrometry method. See Supporting Information sections 2.3 and 2.4 for detailed procedures.

HS-PEG-Peptide Conjugates Synthesis

First, 50 mM HS-PEG-COOH (790 Da) was activated with 500 mM EDC and 1 M NHS in 10 mM MES buffer (pH 5.5) for 30 min. Then, 10 μL of the resulting solution was added to 490 μL of peptide solution (1 mM, PBS 70 mM). The final pH was around 7, and the mixture was stirred overnight.

Enzyme Digestion

Trypsin and RgpB cleavage were both performed with 500 μM PEG-peptide. Typically, 50 μL of PEG-peptide (1 mM) was mixed with 50 μL of buffer (10 mM PBS-pH 7.4 for trypsin and 0.2 M Tris-HCl-pH 7.6, 5 mM $CaCl_2$, 100 mM NaCl, and 40 mM TCEP for RgpB). Then, 10 μL of the enzyme at the appropriate concentration was added. Final concentrations of 2 μM for trypsin and 200 nM for RgpB were used to ensure maximal cleavage. For detection in biofluids, the buffer volume was replaced by an equal volume of biofluid.

Microorganism Culture

Fungal Culture—*In situ* culturing of *C. albicans* (ATCC 90028) from lyophilized stock (KWIK-STIK, VWR) was conducted on Sabouraud dextrose agar plates (Sigma). The plates were then incubated at 30 °C, and pearl-like colonies were observed, indicative of *C. albicans*. Single colonies were then extracted after 2–5 days with sterilized inoculation

loops and inoculated in 3 mL of YEPD medium (2% Bacto peptone, 2% dextrose, 1% yeast extract in H_2O). The inoculates were then grown overnight with gentle shaking at 30 °C. The culture was finally diluted 1:100, and the OD_{600} was measured wherein $OD_{600} = 0.5$ correlates to approximately 1×10^7 cells/mL in 100 μL of RPMI-1640 medium with L-glutamine and 3-(N-morpholino)propane sulfonic acid (MOPS) without sodium bicarbonate, pH 7.0.

Bacteria Cultures—*P. gingivalis* and *F. nucleatum* colonies were grown on brucella blood agar plates (Sigma) from lyophilized stocks of ATCC 33277 and ATCC 25586, respectively (KWIK-STIK, VWR). Anaerobic atmospheres were generated and maintained using anaerobic bags with oxygen indicators (GasPak EZ Pouch System, BD). For *P. gingivalis*, colonies turned black over the following 10 days due to heme accumulation/metabolism (signature of *P. gingivalis*). *F. nucleatum* colonies were faster growing (2–4 days) and maintained a light color. Single colonies were transferred to an enriched tryptic soy broth (eTSB) and grew overnight. The culture was finally diluted, and $OD_{600} = 0.5$ correlates to approximately 1×10^6 cells/mL.

GCF Collection and Testing

The study protocol received approval from the UCSD and USC Institutional Review Boards (Approval HS-19-00163-CR002) and was in accordance with the ethical guidelines for human subjects research established by the Helsinki Declaration of 1975. Subjects were selected from patients receiving dental treatment at the Herman Ostrow School of Dentistry and provided informed consent. Subjects were diagnosed as periodontitis stage III, according to the 2017 World Workshop on the Classification of Periodontal and Peri-implant Diseases and Conditions via extra- and intraoral examination, periodontal probing/examination (clinical attachment level (CAL), tooth mobility, bleeding on probing, gingival biotype), and radiography. Samples were collected using a curet and stored in 250 μL of 20 mM Tris pH 7.4 + 5% glycerol and frozen at −20 °C until use.

Supplementary Material

Refer to Web version on PubMed Central for supplementary material.

ACKNOWLEDGMENTS

REFERENCES

(1). Eke PI; Dye BA; Wei L; Slade GD; Thornton-Evans GO; Borgnakke WS; Taylor GW; Page RC; Beck JD; Genco RJ Update on Prevalence of Periodontitis in Adults in the United States: NHANES 2009 to 2012. J. Periodontol 2015, 86 (5), 611–622. [PubMed: 25688694]

(2). Moore CA; Law JK; Retout M; Pham CT; Chang KCJ; Chen C; Jokerst JV High-Resolution Ultrasonography of Gingival Biomarkers for Periodontal Diagnosis in Healthy and Diseased Subjects. Dentomaxillofacial Radiol. 2022, 51 (6), 20220044.

(3). Dominy SS; Lynch C; Ermini F; Benedyk M; Marczyk A; Konradi A; Nguyen M; Haditsch U; Raha D; Griffin C; Holsinger LJ; Arastu-Kapur S; Kaba S; Lee A; Ryder MI; Potempa B; Mydel P; Hellvard A; Adamowicz K; Hasturk H; Walker GD; Reynolds EC; Faull RLM; Curtis MA; Dragunow M; Potempa J Porphyromonas Gingivalis in Alzheimer's Disease Brains: Evidence for Disease Causation and Treatment with Small-Molecule Inhibitors. Sci. Adv 2019, 5 (1), 1–22.

(4). Hajishengallis G. Periodontitis: From Microbial Immune Subversion to Systemic Inflammation. Nat. Rev. Immunol 2015, 15 (1), 30–44. [PubMed: 25534621]

(5). Hajishengallis G; Lamont RJ Beyond the Red Complex and into More Complexity: The Polymicrobial Synergy and Dysbiosis (PSD) Model of Periodontal Disease Etiology. Mol. Oral Microbiol 2012, 27 (6), 409–419. [PubMed: 23134607]

(6). Byrne SJ; Dashper SG; Darby IB; Adams GG; Hoffmann B; Reynolds EC Progression of Chronic Periodontitis Can Be Predicted by the Levels of Porphyromonas Gingivalis and Treponema Denticola in Subgingival Plaque. Oral Microbiol Immunol 2009, 24 (6), 469–477. [PubMed: 19832799]

(7). Kuboniwa M; Lamont RJ Subgingival Biofilm Formation. Periodontol. 2000 2010, 52 (1), 38–52. [PubMed: 20017794]

(8). Graves D; Jiang Y; Genco C Periodontal Disease: Bacterial Virulence Factors, Host Response and Impact on Systemic Health. Curr. Opin Infect Dis 2000, 13, 227–232. [PubMed: 11964791]

(9). Bostanci N; Belibasakis GN Porphyromonas Gingivalis: An Invasive and Evasive Opportunistic Oral Pathogen. FEMS Microbiol Lett. 2012, 333 (1), 1–9. [PubMed: 22530835]

(10). How KY; Song KP; Chan KG Porphyromonas Gingivalis: An Overview of Periodontopathic Pathogen below the Gum Line. Front Microbiol 2016, 7 (FEB), 1–14. [PubMed: 26834723]

(11). Fitzpatrick RE; Wijeyewickrema LC; Pike RN The Gingipains: Scissors and Glue of the Periodontal Pathogen, Porphyromonas Gingivalis. Future Microbiol 2009, 4 (4), 471–487. [PubMed: 19416015]

(12). Potempa J; Pike R; Travis J Titration and Mapping of the Active Site of Cysteine Proteinases from Porphyromonas Gingivalis (Gingipains) Using Peptidyl Chloromethanes. Biol. Chem 1997, 378 (3–4), 223–230. [PubMed: 9165075]

(13). Potempa J; Pike R; Travis J The Multiple Forms of Trypsin-like Activity Present in Various Strains of Porphyromonas Gingivalis Are Due to the Presence of Either Arg-Gingipain or Lys-Gingipain. Infect. Immun 1995, 63 (4), 1176–1182. [PubMed: 7890369]

(14). Inaba H; Amano A Roles of Oral Bacteria in Cardiovascular Diseases - From Molecular Mechanisms to Clinical Cases: Implication of Periodontal Diseases in Development of Systemic Diseases. J. Pharmacol Sci 2010, 113 (2), 103–109. [PubMed: 20501966]

(15). Lundberg K; Wegner N; Yucel-Lindberg T; Venables PJ Periodontitis in RA-the Citrullinated Enolase Connection. Nat. Rev. Rheumatol 2010, 6 (12), 727–730. [PubMed: 20820197]

(16). Lalla E; Papapanou PN Diabetes Mellitus and Periodontitis: A Tale of Two Common Interrelated Diseases. Nat. Rev. Endocrinol 2011, 7 (12), 738–748. [PubMed: 21709707]

(17). Dominy SS; Lynch C; Ermini F; Benedyk M; Marczyk A; Konradi A; Nguyen M; Haditsch U; Raha D; Griffin C; Holsinger LJ; Arastu-Kapur S; Kaba S; Lee A; Ryder MI; Potempa B; Mydel P; Hellvard A; Adamowicz K; Hasturk H; Walker GD; Reynolds EC; Faull RLM; Curtis MA; Dragunow M; Potempa J Porphyromonas Gingivalis in Alzheimer's Disease Brains: Evidence for Disease Causation and Treatment with Small-Molecule Inhibitors. Sci. Adv 2019, 5 (1), 1–22.

(18). Van Winkelhoff AJ; Van der Velden U; Clement M; De Graaff J Intra-oral Distribution of Black-pigmented Bacteroides Species in Periodontitis Patients. Oral Microbiol. Immunol 1988, 3 (2), 83–85. [PubMed: 3268756]

(19). Aili D; Svärd A; Neilands J; Palm E; Svensater G; Bengtsson T Protein-Functionalized Gold Nanoparticles as Refracto-metric Nanoplasmonic Sensors for the Detection of Proteolytic Activity of Porphyromonas Gingivalis. ACS Appl. Nano Mater 2020, 3 (10), 9822–9830.

(20). Moore C; Cheng Y; Tjokro N; Zhang B; Kerr M; Hayati M; Chang KCJ; Shah N; Chen C; Jokerst JV A Photoacoustic-Fluorescent Imaging Probe for Proteolytic Gingipains Expressed by Porphyromonas Gingivalis. Angew. Chem., Int. Ed 2022, 61 (30), e202201843.

(21). Aldewachi H; Chalati T; Woodroofe MN; Bricklebank N; Sharrack B; Gardiner P Gold Nanoparticle-Based Colorimetric Biosensors. Nanoscale 2018, 10 (1), 18–33.

(22). Lapenna A; Dell'Aglio M; Palazzo G; Mallardi A "Naked" Gold Nanoparticles as Colorimetric Reporters for Biogenic Amine Detection. Colloids Surf., A 2020, 600, 124903.

(23). Jain PK; Huang X; El-Sayed IH; El-Sayed MA Review of Some Interesting Surface Plasmon Resonance-Enhanced Properties of Noble Metal Nanoparticles and Their Applications to Biosystems. Plasmonics 2007, 2, 107–118.

(24). Sharifi M; Attar F; Saboury AA; Akhtari K; Hooshmand N; Hasan A; El-Sayed MA; Falahati M Plasmonic Gold Nanoparticles: Optical Manipulation, Imaging, Drug Delivery and Therapy. J. Controlled Release 2019, 311–312 (June), 170–189.

(25). Khlebtsov NG; Dykman LA Optical Properties and Biomedical Applications of Plasmonic Nanoparticles. J. Quant Spectrosc Radiat Transf 2010, 111 (1), 1–35.

(26). Xu S; Jiang L; Liu Y; Liu P; Wang W; Luo X A Morphology-Based Ultrasensitive Multicolor Colorimetric Assay for Detection of Blood Glucose by Enzymatic Etching of Plasmonic Gold Nanobipyramids. Anal. Chim. Acta 2019, 1071, 53–58. [PubMed: 31128755]

(27). Creyer MN; Jin Z; Retout M; Yim W; Zhou J; Jokerst JV Gold-Silver Core-Shell Nanoparticle Crosslinking Mediated by Protease Activity for Colorimetric Enzyme Detection. Langmuir 2022, 38, 14200–14207. [PubMed: 36351199]

(28). Zhang Y; Jiao J; Wei Y; Wang D; Yang C; Xu Z Plasmonic Colorimetric Biosensor for Sensitive Exosome Detection via Enzyme-Induced Etching of Gold Nanobipyramid@MnO2Nanosheet Nanostructures. Anal. Chem 2020, 92 (22), 15244–15252. [PubMed: 33108733]

(29). Retout M; Mantri Y; Jin Z; Zhou J; Noël G; Donovan B; Yim W; Jokerst JV Peptide-Induced Fractal Assembly of Silver Nanoparticles for Visual Detection of Disease Biomarkers. ACS Nano 2022, 16, 6165. [PubMed: 35377141]

(30). Jin Z; Li Y; Li K; Zhou J; Yeung J; Ling C; Yim W; He T; Cheng Y; Xu M; Creyer MN; Chang YC; Fajtová P; Retout M; Qi B; Li S; O'Donoghue AJ; Jokerst JV Peptide Amphiphile Mediated Co-Assembly for Nanoplasmonic Sensing. Angew. Chem., Int. Ed 2023, 62, e202214394.

(31). Retout M; Valkenier H; Triffaux E; Doneux T; Bartik K; Bruylants G Rapid and Selective Detection of Proteins by Dual Trapping Using Gold Nanoparticles Functionalized with Peptide Aptamers. ACS Sens 2016, 1, 929–933.

(32). Retout M; Blond P; Jabin I; Bruylants G Ultrastable PEGylated Calixarene-Coated Gold Nanoparticles with a Tunable Bioconjugation Density for Biosensing Applications. Bioconjugate Chem. 2021, 32, 290–300.

(33). Retout M; Valkenier H; Triffaux E; Doneux T; Bartik K; Bruylants G Rapid and Selective Detection of Proteins by Dual Trapping Using Gold Nanoparticles Functionalized with Peptide Aptamers. ACS Sens 2016, 1 (7), 929.

(34). Vilela D; González MC; Escarpa A Sensing Colorimetric Approaches Based on Gold and Silver Nanoparticles Aggregation: Chemical Creativity behind the Assay. A Review. Anal. Chim. Acta 2012, 751, 24–43. [PubMed: 23084049]

(35). Jin Z; Mantri Y; Retout M; Cheng Y; Zhou J; Jorns A; Fajtová P; Yim W; Moore C; Xu M; Creyer M; Borum R; Zhou J; Wu Z; He T; Penny W; O'Donoghue A; Jokerst J A Charge-Switchable Zwitterionic Peptide for Rapid Detection of SARS-CoV-2 Main Protease. Angew. Chem., Int. Ed 2022, 61, e202112995.

(36). Jin Z; Ling C; Li Y; Zhou J; Li K; Yim W; Yeung J; Chang Y-C; He T; Cheng Y; Fajtová P; Retout M; O'Donoghue AJ; Jokerst JV Spacer Matters: All-Peptide-Based Ligand for Promoting Interfacial Proteolysis and Plasmonic Coupling. Nano Lett. 2022, 22, 8932. [PubMed: 36346642]

(37). Charbgoo F; Nejabat M; Abnous K; Soltani F; Taghdisi SM; Alibolandi M; Thomas Shier W; Steele TWJ; Ramezani M Gold Nanoparticle Should Understand Protein Corona for Being a Clinical Nanomaterial. J. Controlled Release 2018, 272, 39–53.

(38). Mani E; Lechner W; Kegel WK; Bolhuis PG Equilibrium and Non-Equilibrium Cluster Phases in Colloids with Competing Interactions. Soft Matter 2014, 10 (25), 4479–4486. [PubMed: 24824226]

(39). Retout M; Jin Z; Tsujimoto J; Mantri Y; Borum R; Creyer M; Yim W; He T; Chang Y-C; Jokerst J Di-Arginine Additives for Dissociation of Gold Nanoparticle Aggregates: A Matrix-Insensitive Approach with Applications in Protease Detection. ACS Appl. Mater. Interfaces 2022, 14, 52553–52565. [PubMed: 36346346]

(40). Retout M; Jabin I; Bruylants G Synthesis of Ultra-Stable and Bioconjugable Ag, Au and Bimetallic Ag_Au Nanoparticles Coated with Calix[4]Arenes. ACS Omega 2021, 6, 19675–19684. [PubMed: 34368555]

(41). Gosselin B; Retout M; Dutour R; Troian-Gautier L; Bevernaegie R; Herens S; Lefevre P; Denis O; Bruylants G; Jabin I Ultrastable Silver Nanoparticles for Rapid Serology Detection of Anti-SARS-CoV-2 Immunoglobulins G. Anal. Chem 2022, 94, 7383–7390. [PubMed: 35561247]

(42). Li X; Lenhart JJ; Walker HW Aggregation Kinetics and Dissolution of Coated Silver Nanoparticles. Langmuir 2012, 28 (2), 1095–1104. [PubMed: 22149007]

(43). Agnihotri S; Mukherji S; Mukherji S Size-Controlled Silver Nanoparticles Synthesized over the Range 5–100 Nm Using the Same Protocol and Their Antibacterial Efficacy. RSC Adv. 2014, 4 (8), 3974–3983.

(44). Retout M; Gosselin B; Adrovic A; Blond P; Jabin I; Bruylants G Ultra-Stable Silver Nanoplates: Efficient and Versatile Colorimetric Reporters for Dipstick Assays. Nanoscale 2023, 15, 11981–11989. [PubMed: 37401243]

(45). Retout M; Gosselin B; Mattiuzzi A; Ternad I; Jabin I; Bruylants G Peptide-Conjugated Silver Nanoparticles for the Colorimetric Detection of the Oncoprotein Mdm2 in Human Serum. ChempPlusChem 2022, 87, e202100450.

(46). Lenne Q; Retout M; Gosselin B; Bruylants G; Jabin I; Hamon J; Lagrost C; Leroux YR Highly Stable Silver Nanohybrid Electrocatalysts for the Oxygen Reduction Reaction. Chem. Commun 2022, 58, 3334–3337.

(47). Chang YC; Jin Z; Li K; Zhou J; Yim W; Yeung J; Cheng Y; Retout M; Creyer MN; Fajtová P; He T; Chen X; O'Donoghue AJ; Jokerst JV Peptide Valence-Induced Breaks in Plasmonic Coupling. Chem. Sci 2023, 14, 2659. [PubMed: 36908948]

(48). Moore C; Wing R; Pham T; Jokerst JV Multispectral Nanoparticle Tracking Analysis for the Real-Time and Label-Free Characterization of Amyloid-β Self-Assembly in Vitro. Anal. Chem 2020, 92 (17), 11590–11599. [PubMed: 32786456]

(49). Yang J; Gao Z; Ren X; Sheng J; Xu P; Chang C; Fu Y DeepDigest: Prediction of Protein Proteolytic Digestion with Deep Learning. Anal. Chem 2021, 93 (15), 6094–6103. [PubMed: 33826301]

(50). Rohweder PJ; Jiang Z; Hurysz BM; O'Donoghue AJ; Craik CS Multiplex Substrate Profiling by Mass Spectrometry for Proteases. Methods Enzymol 2023, 682, 375. [PubMed: 36948708]

(51). Houle MA; Grenier D; Plamondon P; Nakayama K The Collagenase Activity of Porphyromonas Gingivalis Is Due to Arg-Gingipain. FEMS Microbiol Lett. 2003, 221 (2), 181–185. [PubMed: 12725924]

(52). Fu L; Ling C; Jin Z; Luo J; Palma-Chavez J; Wu Z; Zhou J; Zhou J; Donovan B; Qi B; Mishra A; He T; Jokerst JV Photoacoustic Imaging of Posterior Periodontal Pocket Using a Commercial Hockey-Stick Transducer. J. Biomed Opt 2022, 27 (05), 1–11.
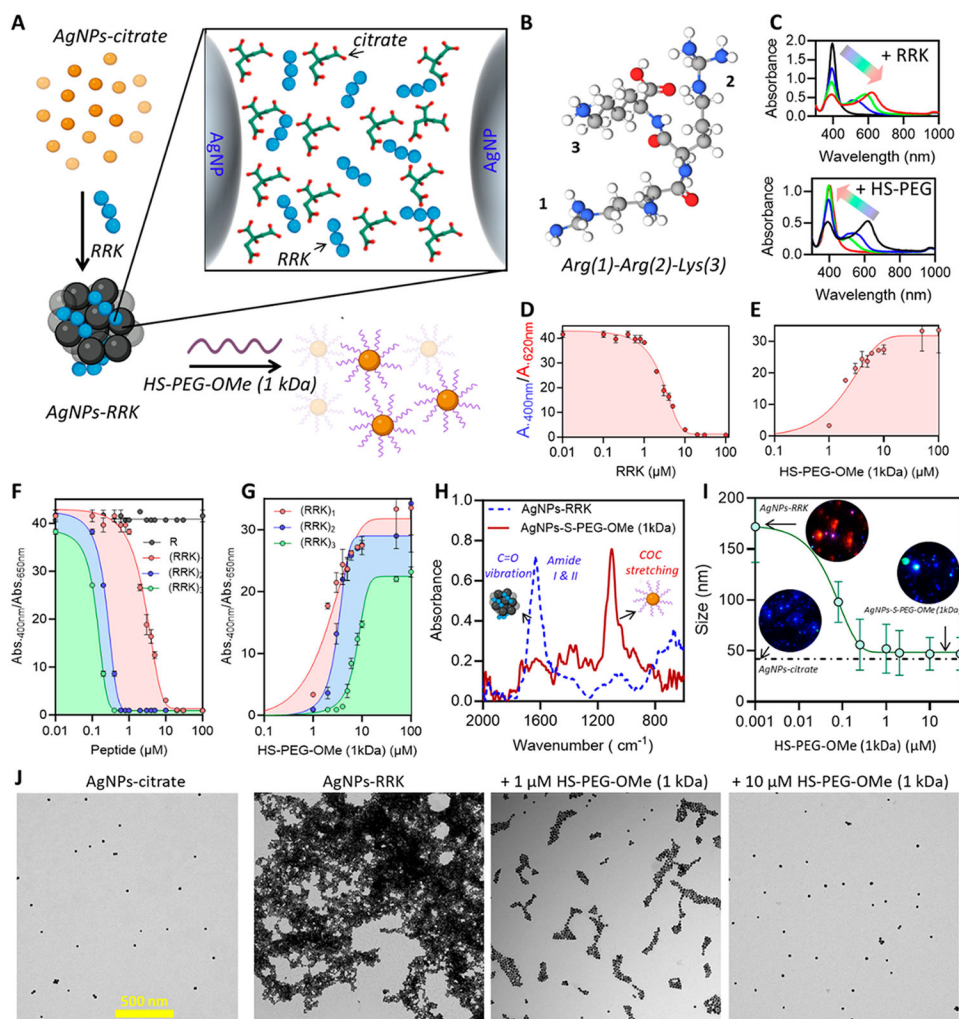
Figure 1.
Reversible assembly of AgNPs. (A) Schematic of the assembly of AgNPs-citrate with addition of the tripeptide RRK and then its dissociation with HS-PEG-OMe (1 kDa). (B) 3D structure of the tripeptide showing the functional groups of the arginine (1, 2) and the lysine (3). Blue = nitrogen, red = oxygen, gray = carbon, and white = hydrogen. (C) UV–vis spectra evolution is through addition of increasing amounts of RRK and increasing concentrations of HS-PEG-OMe (1 kDa) and the corresponding ratio of the absorbances in (D) and (E), respectively. Evolution of the ratio of the absorbances during (F) the assembly of AgNPs with various peptide sequences and their (G) dissociation with HS-PEG-OMe (1 kDa). (H) FTIR spectra of AgNPs-RRK and after dissociation with HS-PEg-OMe (1 kDa) (AgNPs-S-PEG-OMe (1 kDa)). (I) MANTA (dark field) measurements of AgNPs-RRK dissociated with increasing concentrations of HS-PEG-OMe (1 kDa) and (J) corresponding TEM images showing aggregation and dissociation of nanoparticles. Scale bar is 500 nm for every image. The error bars represent the standard deviation of three independent replicates ($n = 3$).
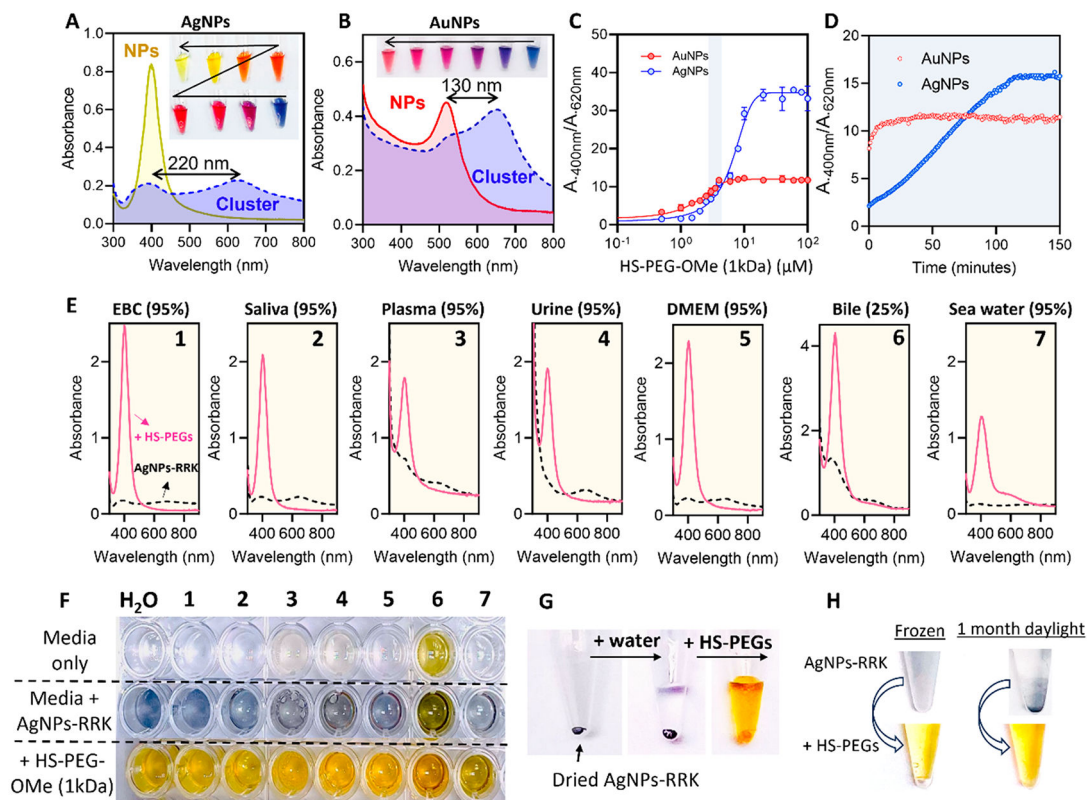
Figure 2.

Colorimetric signal generation of AgNPs. UV–vis spectra of (A) AgNPs-RRK and (B) AuNPs-RRK clusters before and after dissociation in monodispersed NPs with HS-PEG-OMe. Insets show the evolution of the suspension color through the dissociation. (C) Dissociation of AgNPs-RRK and AuNPs-RRK assemblies as a function of the HS-PEG-OMe concentration. (D) Dissociation kinetics for AgNPs-RRK and AuNPs-RRK with 3 μM HS-PEG-OMe. (E) LSPR band of AgNPs-RRK suspended in various media before (black dashed line) and after (pink straight line) dissociation with 20 μM HS-PEG-OMe (1 kDa) and (F) the corresponding pictures; numbers in (F) correspond to sample types listed in (E). (G) Picture of dried AgNPs-RRK and their dissociation with 20 μM HS-PEG-OMe (1 kDa) in water. (H) Pictures of AgNPs-RRK either frozen or left for 1 month on the bench at daylight before and after addition of 20 μM HS-PEG-OMe (1 kDa).
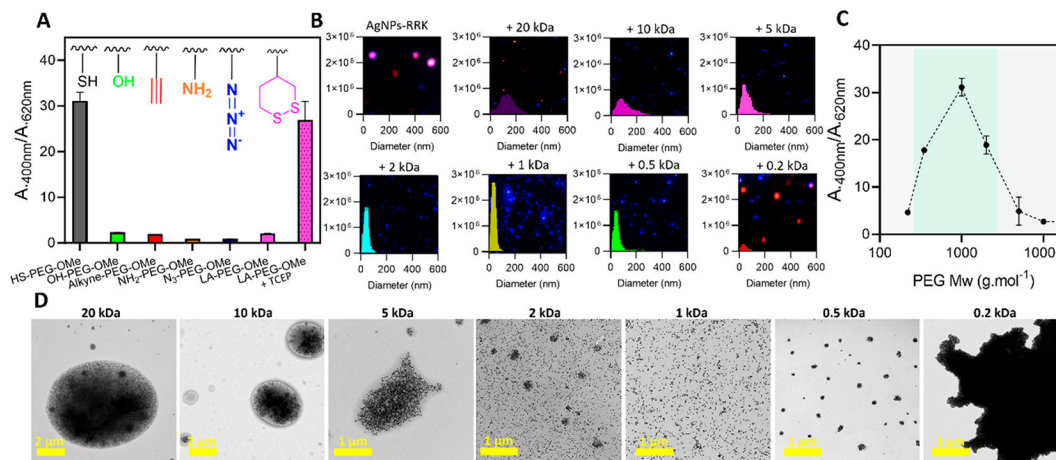
Figure 3.
Structural effect of the PEGs on the dissociation. (A) Ratio of the absorbances of the dissociation induced by PEG-OMe (1 kDa) carrying various anchoring groups. (B) MANTA analysis of the dissociation of AgNPs-RRK aggregates with 10 μM HS-PEG-OMe of different sizes and corresponding (C) ratio of the absorbances and (D) TEM images.
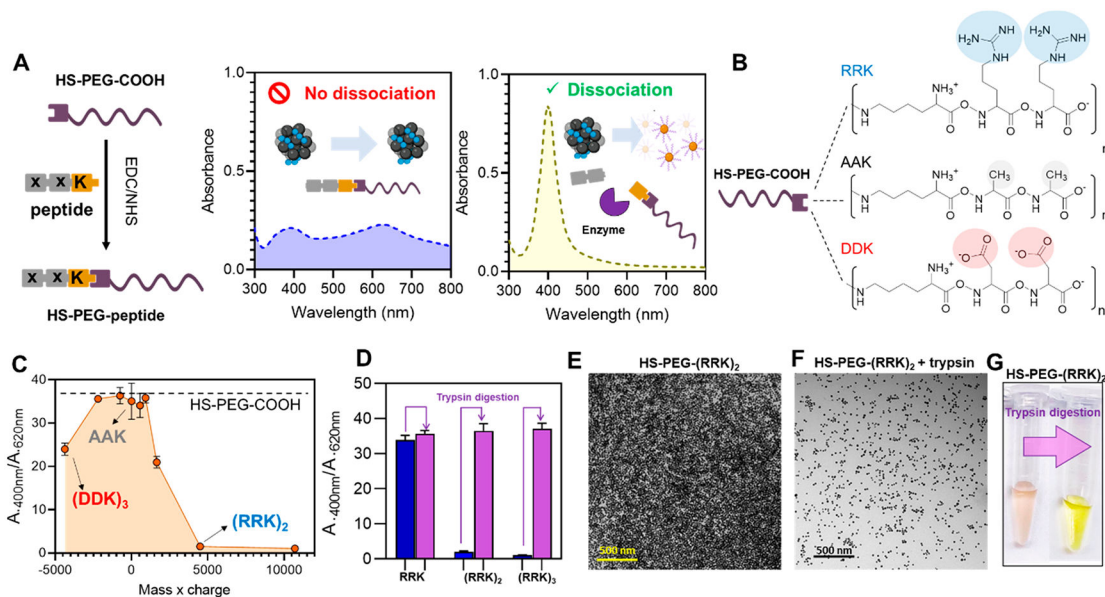
Figure 4.

PEG-peptide study. (A) Illustration of the conjugation of a peptide to a HS-PEG-COOH via EDC/NHS cross-linking. After conjugation, the HS-PEG-peptide cannot dissociate the assemblies. However, in the presence of a specific enzyme, the cleavage restores the dissociation. (B) Structures of the three motifs investigated: AAK, DDK, and RRK. $n = 1$, 2, or 3. (C) Correlation between the dissociation capacity (A_{400nm}/A_{620nm}) and the product mass × charge of the peptide that was conjugated to the HS-PEGs at constant molarity. (D) Restoration of the dissociation capacity of HS-PEG-RRK, -(RRK)$_2$, or -(RRK)$_3$ before and after cleavage by trypsin. (E, F) TEM images of the AgNPs-RRK after the addition of HS-PEG-(RRK)$_2$ incubated or not with trypsin and (G) the corresponding pictures.
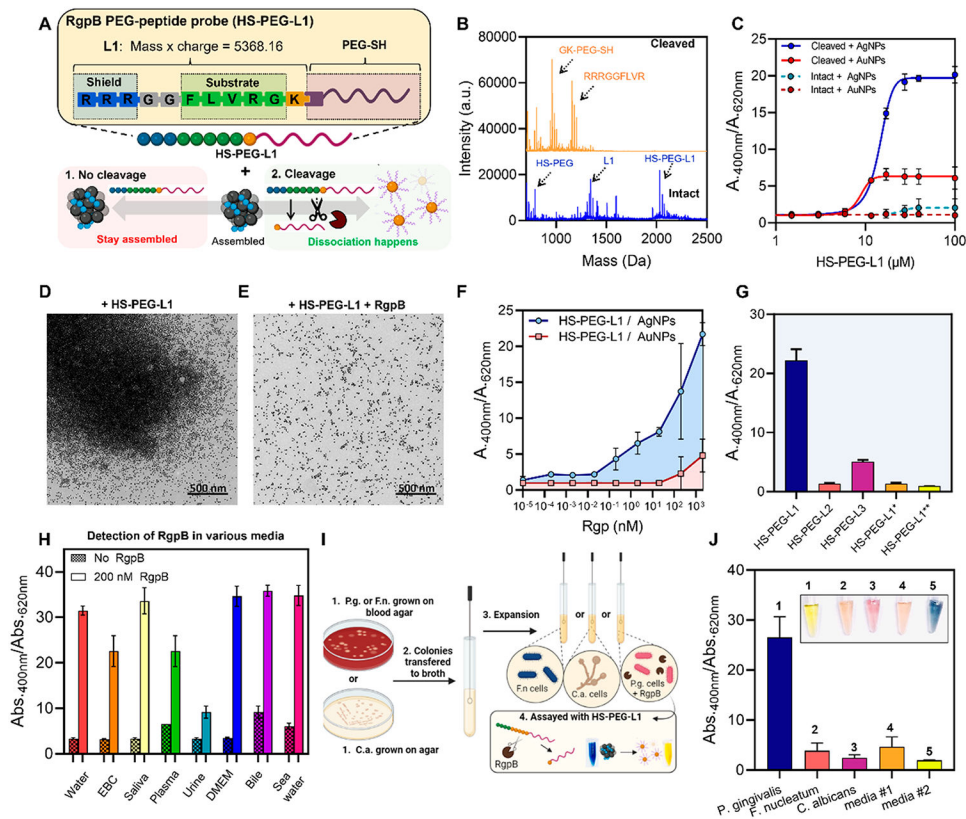
Figure 5.
Design of the PEG-peptide probe specific to gingipains. (A) Scheme of the HS-PEG-peptide probe (HS-PEG-L1) showing the three main parts: the positively charged shield (blue), the peptide substrate (green), and the HS-PEG (purple). In the absence of cleavage, HS-PEG-L1 cannot dissociate the assembly due to the high mass × charge product of L1. However, gingipains expressed by *P. gingivalis* (RgpB) can cleave the peptide substrate after the 4th arginine, resulting in the removal of the peptide fragment from the HS-PEG, and thus the released HS-PEG recovers its dissociation capacity. (B) MALDI-TOF spectra of HS-PEG-L1 intact and cleaved (i.e., after 3 h of incubation with 200 nM RgpB). (C) Ratio of the absorbances of AuNPs (red) or AgNPs (blue) assemblies after the addition of increasing amounts of HS-PEG-L1 either intact (dashed lines) or cleaved (straight lines), and (D) and (E) are the corresponding TEM images, respectively. (F) Ratio of the absorbance of AuNPs (red) or AgNPs (blue) after the addition of HS-PEG-L1 incubated with various concentrations of RgpB. (G) Ratio of the absorbance of control experiments including various HS-PEG-peptide incubated with 200 nM RgpB or HS-PEG-L1 incubated with inactivated RgpB (*heat or **leupeptin). (H) Detection of 200 nM RgpB in various media with HS-PEG-L1. Error bars = SEM. (I) Scheme of the detection of RgpB in bacteria culture and control microorganisms (P.g. = *P. gingivalis,* F.n. = *F. nucleatum*, C.a. = *C. albicans*), and (J) shows the results obtained for the incubation of HS-PEG-L1 in the various cell cultures. Media #1 = bacteria media; media #2 = fungi media.
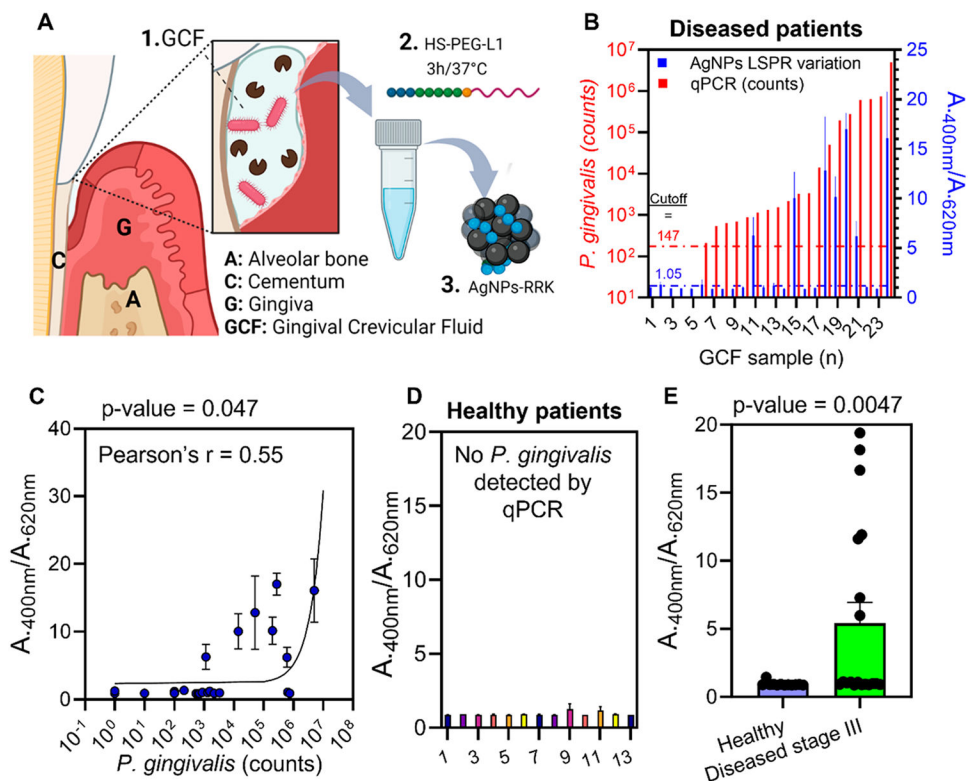
Figure 6.
Clinical sample detection. (A) (1) Illustration of a tooth with periodontal disease and the gingival crevicular fluid (GCF); (2) incubation of GCF with HS-PEG-L1; (3) the addition to the AgNPs-RRK to the GCF/HS-PEG-L1 mixture. (B) Number of *P. gingivalis* cells (red) and LSPR variation (A_{400nm}/A_{600nm}) of the AgNPs-RRK (blue) for each GCF sample (error bars = SD of 3 independent experiment replicates). (C) Correlation between the LSPR variation and the number of *P. gingivalis* cells. (Pearson's $r = 0.55$, two-tailed, $p = 0.0007$). (D) LSPR variation for healthy patients (no *P. gingivalis* detected by qPCR). (E) LSPR variation for individual tooth sites from human subjects as a function of clinically diagnosed periodontal disease (Welch's one-tailed t test, 99% confidence: $p = 0.0047 < 0.01$, error bars = SEM).

Table 1.

RgpB Detection and Control Experiments

name	sequence	feature
L1	Ac-RRRGGFLVRGK	Optimal sequence
L2	Ac-RRRGGFLVAGK	Control substrate
L3	Ac-RRRRRRGGFLVRGK	Increase of the charge
L1*	Ac-RRRGGFLVRGK	Inactivated RgpB
L1**	Ac-RRRGGFLVRGK	Leupeptin present